

Dispersively Probed Microwave Spectroscopy of a Silicon Hole Double Quantum Dot


Rami Ezzouch^{1,*}, Simon Zihlmann¹, Vincent P. Michal², Jing Li², Agostino Aprà¹, Benoit Bertrand³, Louis Hutin³, Maud Vinet³, Matias Urdampilleta⁴, Tristan Meunier⁴, Xavier Jehl¹, Yann-Michel Niquet², Marc Sanquer¹, Silvano De Franceschi^{1,†} and Romain Maurand^{1,‡}

¹Univ. Grenoble Alpes, Grenoble INP, CEA, IRIG-PHELIQS, Grenoble F-38000, France

²Univ. Grenoble Alpes, CEA, IRIG-MEM, Grenoble F-38000, France

³CEA, LETI, Minatec Campus, Grenoble F-38000, France

⁴Univ. Grenoble Alpes, CNRS, Grenoble INP, Institut Néel, Grenoble F-38000, France

 (Received 31 December 2020; revised 6 April 2021; accepted 29 July 2021; published 17 September 2021)

Owing to ever increasing gate fidelities and to a potential transferability to industrial CMOS technology, silicon spin qubits have become a compelling option in the strive for quantum computation. In a scalable architecture, each spin qubit will have to be finely tuned and its operating conditions accurately determined. In view of this, spectroscopic tools compatible with a scalable device layout are of primary importance. Here we report a two-tone spectroscopy technique providing access to the spin-dependent energy-level spectrum of a hole double quantum dot defined in a split-gate silicon device. A first gigahertz-frequency tone drives electric dipole spin resonance enabled by the valence-band spin-orbit coupling. A second lower-frequency tone (approximately 500 MHz) allows for dispersive readout via rf-gate reflectometry. We compare the measured dispersive response to the linear response calculated in an extended Jaynes-Cummings model and we obtain characteristic parameters such as g factors and tunnel and spin-orbit couplings for both even and odd occupation.

DOI: [10.1103/PhysRevApplied.16.034031](https://doi.org/10.1103/PhysRevApplied.16.034031)

I. INTRODUCTION

Single spins localized in gate-defined quantum dots have been recognized as a promising platform for quantum computation early on [1]. Among them, spin qubits in silicon have attracted a lot of interest due to their long coherence [2] and possibility of single- [3] and two-qubit gates [4]. The steady evolution towards increasing the number of qubits has triggered the quest for a compact control and readout architecture. Considering qubit control, all electrical qubit driving appears as a clear asset in dense quantum dot arrays and has been investigated with intrinsic or artificial spin-orbit interaction either in silicon [2,5,6] or germanium [7–9]. For readout, the commonly used spin-to-charge conversion with subsequent charge detection through nearby charge sensors is becoming increasingly challenging as the number of quantum dots to sense increases [10,11]. Gate-based dispersive readout [12,13] is an alternative strategy possibly usable for a dense array [14]. It benefits in particular from large gate lever arms [15–17] and single-shot readout has been demonstrated

[18–20] with a fidelity up to 98% for 6 μ s integration time with on-chip resonators [14]. Despite all the advantages of gate-based dispersive readout of the charge qubit directly, it also has its limitations. One of the main drawbacks is the limited information that the fundamental energy spectrum of each qubit gate-based dispersive readout is able to provide compared to commonly used transport or charge sensing. This includes trivial quantities such as gate lever arms and charge tunnel couplings in general, but also quantum dot level spacings and, in particular, for spin-orbit qubits, the g factor and spin-orbit interaction strength. Moreover, charge sensing gives direct access to the number of charges and hence the parity of the charge state in a double quantum dot, which is not the case for gate-based dispersive readout. However, dispersive readout coupled with microwave spectroscopy has been proven to be a powerful tool to access some of this information, among them lever arm [21] and charge tunnel coupling [21,22].

With the rapid progress of hole spin qubits in silicon [6,17,23] and germanium [7–9,11,24], there is a strong need to characterize and explore these qubits. Not only do hole spin qubits allow for a dense integration of qubits [11] while preserving individual addressability [6,25], but there is plenty of physics in the interplay of orbital and spin degree of freedom to discover.

*rami.ezzouch@cea.fr

†silvano.defranceschi@cea.fr

‡romain.maurand@cea.fr

Here we perform a two-tone magnetospectroscopy on a hole silicon double quantum dot (DQD) as a model system. Because of spin-orbit interactions, spin-flip photon-assisted tunneling is possible under microwave irradiation and detectable by gate-based dispersive readout. The spectroscopy then allows the reconstruction of the entire energy spectrum of the DQD necessary for qubit control and readout. A qubit-driven Jaynes-Cummings Hamiltonian resolved in the linear regime is supporting our experimental findings.

II. METHODS

The experiment is realized in a *p*-type double gate MOS-FET fabricated on a 300 mm silicon-on-insulator wafer using an industry-standard fabrication line [6,26]. The silicon channel is nominally 10 nm thick, 80 nm wide, and is partially overlapped by two 32 nm long gates [see the inset of Fig. 1(a) for an electron micrograph of a nominally identical device]. The gates are defined by *e*-beam lithography and have enlarged SiN spacers to avoid doping implantation in the channel. This face-to-face geometry allows the accumulation of a hole DQD in parallel (with the source and drain) by applying negative dc voltages V_{G1} and V_{G2} on the gates when the device is operated in a dilution refrigerator at the base temperature $T_{\text{base}} = 30$ mK. The two dots are formed at the corners of the channel overlapped by the gates [26]. Figure 1(a) schematically shows the device as well as its gate connections. Gate 2 as well as the drain (not shown) are connected to a broadband high-frequency coaxial line that allows us to perform microwave two-tone spectroscopy. Gate 1 is connected to a surface mount inductor ($L = 220$ nH), which forms with its parasitic capacitance ($C_p = 466$ fF) and device impedance an LC resonator with a resonance frequency $f_r = \omega_r/(2\pi) = 497$ MHz, a loaded quality factor $Q_{\text{loaded}} \approx 24$ and a characteristic impedance $Z_c = 2\pi f_r L \approx 700 \Omega$ [27].

The hole DQD acts as a variable load for the LC resonator and the resonance frequency undergoes a dispersive shift depending on the DQD state. This can be readily understood if one considers a $(M+1, N) \leftrightarrow (M, N+1)$ interdot charge transition with M (N) the charge number in the left (right) dot. The two-state Hamiltonian of this system reads $H_{\text{DQD}} = -\varepsilon\sigma_z/2 - \Delta\sigma_x/2$, where the Pauli matrices act in the space of the charge configuration. Here σ_x describes the tunneling between the dots that opens a gap Δ in the energy spectrum. The difference in energy of the two states reads $E = \sqrt{\varepsilon^2 + \Delta^2}$ and is a function of the detuning ε . In the adiabatic limit, when the resonator angular frequency $\omega_r \ll E/\hbar$, the interaction between a charge qubit and a resonator has often been treated semiclassically with the introduction of quantum capacitances [28–30]. However, when the frequency of the readout oscillator is comparable to the characteristic frequency of the measured

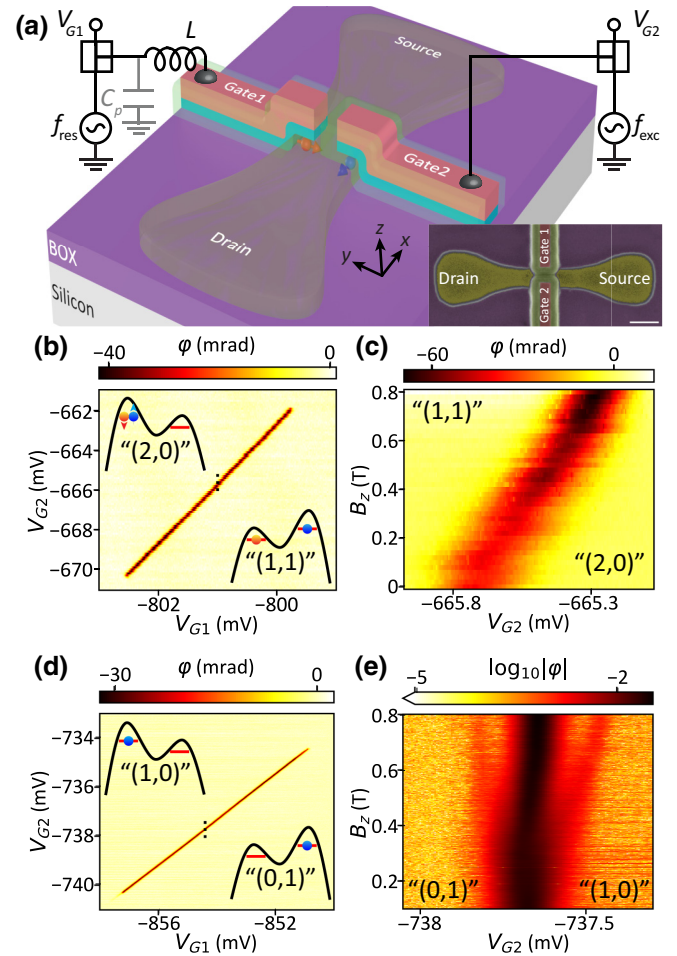


FIG. 1. Double quantum dot device and working points. (a) Simplified 3D schematic of a split-gate, silicon-on-insulator field-effect transistor. An LC resonator wired to gate 1 is used for reflectometry readout. Static voltages V_{G1} and V_{G2} are applied to gates 1 and 2. Using bias tees, they are combined with about a 500 MHz reflectometry tone (f_r) and a 1–20 GHz microwave spectroscopy tone (f_{exc}), respectively. The inset shows a false color scanning electron micrograph of the device (scale bar is 100 nm). (b),(d) Phase response of the LC resonator as a function of V_{G1} and V_{G2} showing interdot charge transitions ICT 2 and ICT 3 for even and odd parities, respectively. The insets show the equivalent one- and two-electron charge configurations just above and below ICT 3 and ICT 2, respectively. The first (second) number represents the equivalent hole occupation in the dot under gate 1 (gate 2). (c),(e) Phase response as a function of V_{G2} and B_z at fixed V_{G1} [see the dashed lines in (b) and (d)], revealing the ground-state evolution in the magnetic field.

system ($\omega_r \simeq E/\hbar$), a quantum mechanical treatment of the interaction with an extended Jaynes-Cummings Hamiltonian is convenient in order to take into account the finite frequency of the readout apparatus. Recently, it was shown that, for a charge qubit, such a model also captures the interaction in the adiabatic limit [31]. Here, we therefore model all the interactions within the framework of the

Jaynes-Cummings Hamiltonian. This quantum approach provides complementary physical insights and proves useful in describing more complex situations. In particular, we extend the Jaynes-Cummings model to the driven case (with microwaves at frequency f_{exc}), where we also capture dispersive shifts due to resonantly driven transitions between states in the DQD (a complete discussion of the underlying theory can be found in Appendix A).

The coupling between the DQD and the readout resonator, described by the Hamiltonian $H_r = \hbar\omega_r(a^\dagger a + 1/2)$, is expressed in the basis of the charge configurations as $H_{\text{int}} = \hbar g_c \sigma_z (a + a^\dagger)$, with a the annihilation operator of the oscillator, $g_c = (\alpha_1 - \alpha_2)eV_{\text{rms}}/(2\hbar)$ the coupling strength between the charge and the microwave photons, and $V_{\text{rms}} = \sqrt{\hbar\omega_r/(2C_r)}$ the zero-point voltage fluctuation of the LC oscillator, where C_r is the capacitance of the LC circuit (which includes the geometric capacitance of the DQD). The coupling between gate 1 and the double quantum dot charge leads to a phase shift between the incoming and the reflected microwaves. In the linear regime discussed in Appendix A, the phase shift can be expressed as

$$\delta\phi = \frac{4Q_{\text{loaded}}\text{Re}\chi(\omega_r)}{\omega_r}, \quad (1)$$

where $\chi(\omega_r)$ is the charge response function whose real part represents the linear shift in the resonant angular frequency of the LC circuit. For a pair of states near charge degeneracy with the readout oscillator in the adiabatic limit, the response function is real and equal to

$$\chi = -\frac{2\hbar g_c^2 \Delta^2}{(\varepsilon^2 + \Delta^2)^{3/2}}, \quad k_B T, \hbar\omega_r, \hbar\Gamma_2 \ll \Delta, \quad (2)$$

where k_B is the Boltzmann constant, T is the equilibrium temperature of the DQD environment, and Γ_2 is the decoherence rate of the DQD charge. Equation (2) is equivalent to the standard oscillator shift $\delta\omega_r = -C_Q\omega_r/(2C_r)$, with C_Q the quantum capacitance of the DQD [13,22,30].

III. RESULTS

When measuring the phase response of the resonator at its resonance frequency while sweeping the gate voltages V_{G1} and V_{G2} , we obtain the charge stability diagram of the DQD system [27]. Diagonal features with positive slope in this diagram mark interdot charge transitions (ICTs). This work is focused on three interdot transitions, ICT 1 and ICT 2 on device 1 and ICT 3 on device 2, all chosen to have an estimated hole number below 20 in each dot. Figures 1(b) and 1(d) show the stability diagrams around ICT 2 and ICT 3, respectively. For the case of ICT 1, see the Supplemental Material [27]. Using the model introduced above and fitting the phase response as a function

of detuning at each ICT, we find a charge-photon coupling $g_c/(2\pi) \simeq 35$ MHz for all three interdot transitions; see Appendix B 3.

Any given ICT is characterized by either an even or an odd parity of the total occupation number in the DQD. Without knowing this number, different parities can still be discriminated through the magnetic field evolution of the corresponding ICT phase response [12,32–34].

A. Parity of the DQD

For holes in silicon, the presence of spin-orbit interaction changes the magnetic field dependence of the ICT as spin-flip tunneling is allowed and couples different spin states. However, we show in the next paragraph that it is still possible to infer the interdot charge parity from the dispersive response in the magnetic field. The phase response of the LC resonator is measured as a function of V_{G2} and the magnetic field, keeping V_{G1} constant. Measurements are shown in Figs. 1(c) and 1(e).

In the even case, Fig. 1(c), the dip in phase at zero detuning and zero magnetic field arising from the avoided crossing of the $S(1,1) \leftrightarrow S(2,0)$ remains unchanged as long as the Zeeman energy of the polarized triplet state $E_Z < \Delta$. Once E_Z becomes larger than Δ , the state $|\downarrow\downarrow\rangle$ becomes the ground state in the $(1,1)$ configuration and a new avoided crossing mediated by spin-orbit interaction between $|\downarrow\downarrow\rangle$ and $S(2,0)$ emerges, which we characterize by an energy gap Δ_{SO} ; see Fig. 3(c) for an energy diagram at finite magnetic field. With increasing magnetic field, this avoided crossing moves towards higher detuning, which explains why the dip in phase in Fig. 1(c) moves towards larger V_{G2} as the magnetic field is increased. Moreover, the increase in phase shift is due to $\Delta_{\text{SO}} < \Delta$, which gives rise to a higher dispersive shift χ at higher field following Eq. (2). We stress that the situation described here is different from a previously reported situation of a hole DQD in silicon [17]. There, the negligible Δ_{SO} paired with a Δ comparable to temperature led to the thermal population of higher lying states, which themselves led to a dispersive shift of the resonator.

In the odd case, Fig. 1(e), the central dip in phase does not vary much with increasing magnetic field, indicating that the nature of the ground state is unchanged. However, Fig. 1(e) shows two additional phase signals appearing on either side of the central phase dip. These originate from higher-lying avoided crossings in the DQD level spectrum that lead to nonzero electric susceptibility; see Fig. 4(b) for an energy diagram at finite magnetic field. Their origin is the spin-orbit mediated coupling of states with opposite spins in the two dots. With increasing magnetic field, these dips in phase move away from the central feature and fade out. The dispersion is again linked to a change in E_Z , whereas the reduced phase signal is explained by a lower

occupation probability of the excited state by thermal activation. The slight dispersion of the central dip arises from a difference in the Landé g factors of the two QDs. The dispersive detection of higher-lying avoided crossings due to spin-orbit interaction is similar to the recently reported observation of valley splittings in cavity-coupled electron quantum dots in silicon [35].

B. Spectroscopy at zero magnetic field

Having established the parity of each ICT, we proceed to microwave spectroscopy to explore the full DQD level spectrum as a function of magnetic field, B_z , along the z axis, i.e., perpendicular to the substrate. Both even and odd charge configurations have two anticrossing states, with doublet and single spin character, respectively. The even configurations are characterized by the additional presence of spin-triplet states, which can be neglected at zero magnetic field because of their negligible dispersive shift. As a result, in both even and odd cases, a single charge tunnels between the two QDs, giving rise to a nonzero electric susceptibility at the ICT; see Eq. (2). We can extend this model to capture microwave photon-induced tunnel events by adding a fast electrical drive $A_{\text{exc}} \cos(\omega_{\text{exc}} t)/2$ to gate 2. The Hamiltonian describing the full system now also includes $H_{\text{exc}} = A_{\text{exc}} \cos(\omega_{\text{exc}} t) \sigma_z/2$, where A_{exc} is the amplitude of the fast drive signal. By solving the complete Hamiltonian $H = H_{\text{DQD}} + H_{\text{exc}} + H_r + H_{\text{int}}$, we find a linear response function

$$\chi(\omega_r) = - \left[- \frac{2\hbar g_c^2 \Delta^2 \delta\omega}{E^3 \omega_R} + \left(g_c \frac{\varepsilon \omega_{R0}}{E \omega_R} \right)^2 \frac{1}{\omega_R - \omega_r - i\tilde{\Gamma}_2} \right] D, \quad (3)$$

where $\delta\omega = \omega_{\text{exc}} - E/\hbar$ is the detuning of the drive frequency ω_{exc} from the DQD transition energy E , $\omega_R = \sqrt{\delta\omega^2 + \omega_{R0}^2}$ is the Rabi frequency due to the resonant drive with $\omega_{R0} = A_{\text{exc}} \Delta / (2\hbar E)$, $\tilde{\Gamma}_2$ is the decoherence rate of the driven system, and D is the difference in the occupation probabilities of the ground and excited states in the dressed basis. The first term is the adiabatic response already described in Eq. (2), whereas the second term now includes the dispersive shift due to resonantly driven charge transitions in the DQD. Let us note that in Eq. (3) we have only retained the rotating wave approximation (RWA) contribution of the resonant term that we expect to be a good approximation in a quite extended range of dot detuning. Otherwise the non-RWA contribution may also be included straightforwardly. A detailed derivation of Eq. (3) is given in Appendix A.

Figure 2(a) shows the phase response of the even-parity ICT 2 as a function of V_{G2} and $f_{\text{exc}} = \omega_{\text{exc}} / (2\pi)$ for fixed V_{G1} . Qualitatively similar results can be found for odd

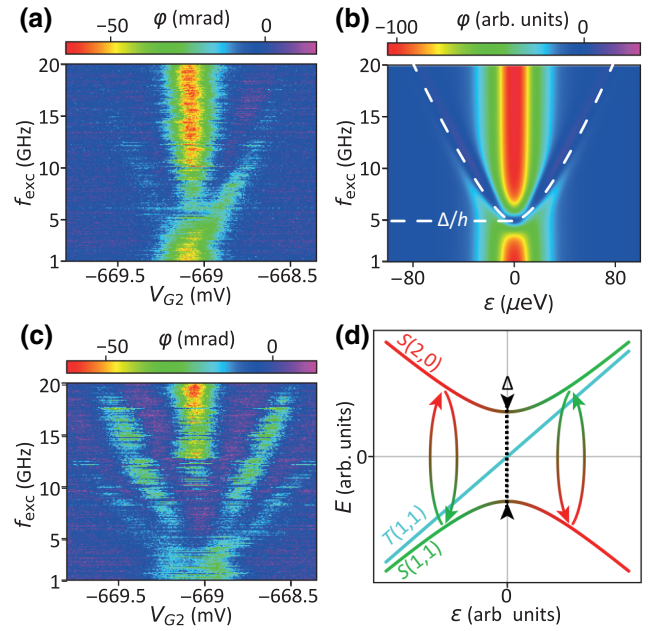


FIG. 2. Photon-assisted spectroscopy at zero magnetic field. (a) Phase response of the resonator as a function of gate voltage, V_{G2} , and microwave frequency, f_{exc} , at zero magnetic field. The output power of the microwave generator is adjusted for each f_{exc} in order to deliver a constant power at the device [27]. We estimate the power at the device level to be around -70 dBm. In addition to the central interdot transition signal vanishing at 5.72 ± 0.04 GHz, two side branches mark photon-assisted charge transitions between the quantum dots. (b) Theoretical simulation of the driven DQD phase response. The central dip at $\varepsilon = 0$ vanishes when the excitation energy matches Δ . (c) Multiphoton processes arising at higher driving power. The delivered microwave power is increased by 10 dBm compared to (a). Additional side branches appear at one-half and one-third of the side-branch frequency in (a), indicating two-photon and three-photon processes, respectively. (d) Energy diagram of a DQD near the “(1,1)” \leftrightarrow “(2,0)” transition at zero magnetic field. The double arrows mark the processes giving rise to the branches observed in (a).

parity cases, such as ICT 3 (not shown). To analyze the data in Fig. 2(a), we refer to the corresponding energy diagram at zero magnetic field, shown in Fig. 2(d). Resonant microwave-induced transitions are highlighted by double arrows at positive and negative detuning.

The vertical ridge at $V_{G2} \simeq -669.1$ mV corresponds to the dispersive shift arising from the charge qubit associated with the $S(1,1)$ - $S(2,0)$ anticrossing as described by the first term in Eq. (3). The phase dip along this line vanishes when the microwave excitation energy matches the energy gap Δ due to tunnel coupling, i.e., when $\delta\omega \rightarrow 0$ [21,22,33]. From this we find that $\Delta/\hbar = 5.72 \pm 0.04$ GHz (see Appendix B 1)

Two side branches can be seen in the the same figure. They consist of dip-peak features due to microwave-assisted excitation away from the charge degeneracy point

at $\epsilon = 0$. They occur when the microwave tone is in resonance with the charge qubit energy E , once again when $\delta\omega \rightarrow 0$. and they are accounted for by the second term in Eq. (3).

At large detuning ($\epsilon \gg \Delta$), the side branch turns into straight lines whose slopes can be used to extract the lever-arm parameter $\alpha_2 = 0.160 \pm 0.001$, relating the detuning energy to the gate 2 voltage; see Appendix B 2. From the slope of the ICT 2 line in Fig. 1(b), we can further infer the lever-arm parameter for gate 1, $\alpha_1 = 0.50 \pm 0.02$.

The data in Fig. 2(a) show a clear asymmetry between the two branches, with the branch at positive detuning being more pronounced. This asymmetry may be ascribed to the presence of the triplet states, which affects the population of the anticrossing singlet states. At negative detuning, the $S(1,1)$ ground state is partially depopulated due the thermal population of the closely lying triplet excited states. This should lead to a fainter side branch since the triplets do not contribute any measurable dispersive phase shift and cannot be photon excited to the $S(2,0)$ state due to time-reversal symmetry at zero magnetic field.

Using the model introduced above, we can qualitatively reproduce the experimental results, as shown in Fig. 2(b), where the transition energy E is highlighted by a white dashed line. The exact shape of the dip-peak phase branches that emerge when the charge qubit is driven resonantly at nonzero detuning is a sensitive function of dephasing and relaxation whose complete modeling goes beyond the scope of this work.

When the system is strongly driven, multiphoton processes can occur ($nhf_{\text{exc}} = E$, where n is an integer). Figure 2(c) shows the phase response at large microwave power. In addition to the dispersive shift of the driven charge qubit originating from a one-photon process, new branches appear at half and one-third the frequencies of the original branches, demonstrating two- and three-photon processes, respectively. The theoretical description of the multiphoton case can be found in Appendix A 7.

To sum up, microwave spectroscopy at zero magnetic field is a powerful tool to extract the interdot charge tunnel coupling as well as the lever-arm parameters for both gates, allowing the reconstruction of the DQD spectrum at zero magnetic field.

C. Spectroscopy of a DQD with an even charge configuration at finite magnetic field

We now proceed with microwave spectroscopy at finite magnetic field to explore the spin-split energy levels and the spin-orbit coupling in the DQDs. First, we present results for ICT 2. At an external magnetic field $B_z = 600$ mT, the triplet states split, leading to a DQD energy spectrum as illustrated in Fig. 3(c), where the $|\downarrow\downarrow\rangle$ is the ground state at $\epsilon = 0$. Because of a difference in g factors between the two quantum dots, the $T_0(1,1)$ state

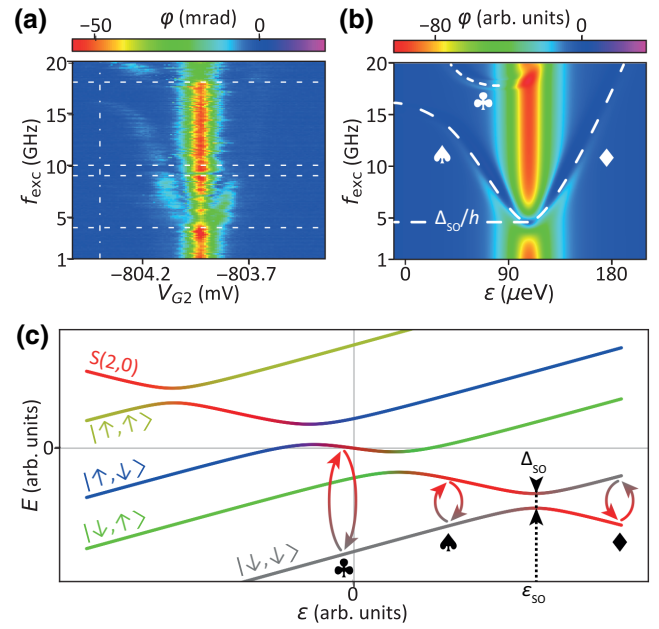


FIG. 3. Photon-assisted spectroscopy at finite magnetic field for an even-parity interdot charge transition. (a) Phase response of the LC resonator around the spin-orbit anticrossing of $|\downarrow\downarrow\rangle$ with $S(2,0)$ as a function of V_{G2} and f_{exc} at $B_z = 600$ mT. The dashed horizontal lines delimit regions in which the spectroscopy tone power is held constant at room temperature. The dash-dot vertical line marks the position of the ICT at zero magnetic field, corresponding to $\epsilon = 0$. The strong vertical structure is associated with the spin-orbit anticrossing at $\epsilon = \epsilon_{\text{SO}}$. It vanishes at $f_{\text{exc}} = \Delta_{\text{SO}}/h = 4.6 \pm 0.1$ GHz. The three side branches around the central signal correspond to photon-induced charge transitions between the quantum dots, as indicated in (c). (b) Corresponding simulated phase response of the driven DQD. (c) Energy diagram of DQD of around a “(1,1)” \leftrightarrow “(2,0)” transition at finite magnetic field and with $g_1 \neq g_2$. The photon-induced charge transitions responsible for the side branches in (a) and (b) are indicated by arrows and corresponding symbols.

mixes with the singlet $S(2,0)$ state around $\epsilon = 0$ and a new basis for the (1,1) states consisting of four nondegenerate states, $|\downarrow\downarrow\rangle$, $|\uparrow\downarrow\rangle$, $|\downarrow\uparrow\rangle$, and $|\uparrow\uparrow\rangle$, needs to be adopted. At positive detuning, $|\downarrow\downarrow\rangle$ and $S(2,0)$ couple due to the intrinsic spin-orbit coupling in the valence band of silicon. At finite magnetic field, this gives rise to an avoided crossing Δ_{SO} with characteristic energy Δ_{SO} at a magnetic-field-dependent detuning $\epsilon = \epsilon_{\text{SO}}$.

Around ϵ_{SO} , the hole DQD could be operated as a “spin-flip” charge qubit. In Fig. 3(a), we show a two-tone spectroscopy around $\epsilon = \epsilon_{\text{SO}}$. The dispersive interaction of the qubit with the resonator gives rise to the vertical dip structure at $V_{G2} \simeq -803.9$ mV. As for the case of a spinless charge qubit (Fig. 2), we observe a local suppression of this dip structure from which we extract a spin-orbit-mediated avoided crossing $\Delta_{\text{SO}}/h = 4.6 \pm 0.1$ GHz (see Appendix B 1).

Away from ε_{SO} , the dispersive shift due to the driven “spin-flip” charge qubit arises when the microwave photon energy matches the energy splitting between $S(2,0)$ and $|\downarrow\downarrow\rangle$. Close to $V_{G2} = -804.2$ mV, i.e., close to zero detuning, the left branch bends towards a horizontal asymptote around 16 GHz. This arises from the hybridization of the excited state $S(2,0)$ with the $|\downarrow\uparrow\rangle$ state, as shown in Fig. 3(c). In this regime, the “spin-flip” charge qubit evolves to a single-dot “spin-orbit” qubit for which the electric dipole is largely reduced and cannot be sensed by the LC resonator. From the frequency of the horizontal asymptote we extract the g factor of the second dot, $g_2 = 1.92 \pm 0.02$. At $V_{G2} = -804.2$ mV and for frequencies close to 20 GHz, an additional phase signal is visible in Fig. 3(a). This signal can be associated with the transition between $|\downarrow\downarrow\rangle$ and the hybridized $S(2,0)$ and $|\uparrow\downarrow\rangle$ states. In principle, this branch could allow for the extraction of the g factor of the first dot. However, due to the upper limit of 20 GHz in our microwave generator, we are not able to fully capture this feature and we only infer $g_1 > 2.38$.

Similarly to the zero magnetic field case, the dispersive shift of the resonator can be modeled by also taking into account the spin degree of freedom as well as the spin-orbit interaction. Apart from spin-flip tunnel events, the physics remains the same. We again find qualitative agreement with the measurements; see Fig. 3(b). The white dashed lines highlight the transition energies as indicated with different arrows in Fig. 3(c). We again note that the exact shape of the side wings depends on the details of the decoherence of the driven system and therefore exact modeling goes beyond the scope of this work.

D. Spectroscopy of a DQD with an odd charge configuration at finite magnetic field

We now present in Fig. 4 microwave spectroscopy measurements for ICT 3, the odd-parity ICT. At finite magnetic field the basis states $|L\rangle$ and $|R\rangle$ of an odd parity ICT are spin split into $|L\downarrow\rangle$, $|L\uparrow\rangle$, $|R\downarrow\rangle$, and $|R\uparrow\rangle$, resulting in the energy diagram of Fig. 4(b). Around zero detuning, pure charge tunnel coupling gives rise to avoided crossings between states with the same spin, i.e., between $|L\downarrow\rangle$ and $|R\downarrow\rangle$ and between $|L\uparrow\rangle$ and $|R\uparrow\rangle$. The strong central feature in Fig. 4(a) is due to the dispersive shift associated with the lowest energy one, involving spin-down states.

Similar to the even-parity case, two side branches arise when hf_{exc} matches the energy difference between ground and excited states, corresponding to transitions from $|L\downarrow\rangle$ to $|R\downarrow\rangle$ and vice versa. They exhibit clear avoided crossings around 12 GHz. The one on the left (right) is due to a spin-orbit-mediated tunnel coupling between $|L\uparrow\rangle$ and $|R\downarrow\rangle$ ($|L\downarrow\rangle$ and $|R\uparrow\rangle$). We note that the observed branches, highlighted by white dashed lines, are in fact

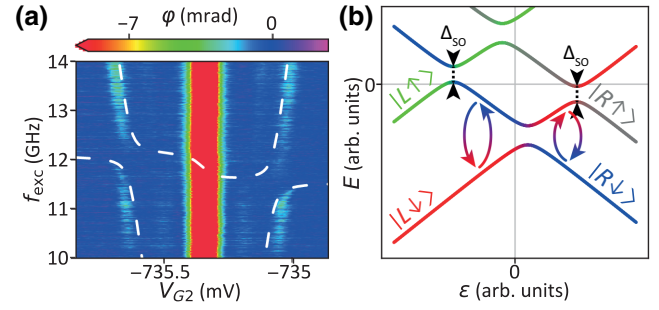


FIG. 4. Photon-assisted spectroscopy at finite magnetic field for an odd-parity interdot charge transition. (a) Phase response of the LC resonator around zero detuning as a function of V_{G2} and f_{exc} at $B_z = 1.3$ T. The dispersive response due to the charge qubit is visible as the vertical feature at $V_{G2} \approx -737.3$ mV. At resonance, $2hf_{exc} = \Omega$, the resonator also undergoes a phase shift (white dashed line). Around 12 GHz, spin-orbit anticrossings between states with opposite spin localized in different dots are detectable in the driven response. (b) Energy diagram of a single hole in a DQD [“(0,1)” \leftrightarrow “(1,0)” transition] at finite magnetic field with $g_1 \simeq g_2$. At zero detuning, the down spin states of the left and right dots undergo an anticrossing due to tunneling t . A small anticrossing due to the spin-orbit interaction appears between the down spin states of one dot and the up spin states of the other dot. Microwave-induced transitions that give rise to the two branches are highlighted with arrows.

due to two-photon excitations. As a consequence, transition frequencies in Fig. 4(a) are a factor of 2 smaller than the actual transition energies. The resonant line originating from the one-photon process is faintly visible between the main vertical feature and the discussed wings. From the amplitude of the measured avoided crossings we find a spin-orbit gap $\Delta_{SO}/h = 2.4$ GHz. In addition, the side branch on the left (right) asymptotically approaches a constant frequency set by the Zeeman energy in the left (right) quantum dot. This allows us to determine the two g factors of the DQD, which happen to differ slightly from each other, i.e., $g_L = 1.27$ and $g_R = 1.33$.

IV. CONCLUSIONS

In conclusion, we have performed microwave magnetospectroscopy in combination with gate-based dispersive readout of silicon hole DQDs. By modeling the DQD coupled to the LC resonator and microwave spectroscopic tone by a driven Jaynes-Cummings Hamiltonian, we derive the linear response function of the system, which qualitatively explains our experimental data. Because of the spin-orbit interaction present in the valence band of silicon, all spin-orbit states have been revealed by two-tone spectroscopy, enabling a precise reconstruction of the DQD energy diagram in both even- and odd-parity interdot transitions. Consequently, we are able to extract all of necessary physical parameters of a DQD, i.e., gate lever arms, tunnel

couplings, g factors, and spin-orbit strength. The demonstrated two-tone spectroscopy combined with frequency multiplexed gate dispersive readout could enable parameter characterization in dense arrays of spin-orbit qubits without the need for local charge detectors and reservoirs whose integration is technically challenging. Moreover, the use of superconducting LC resonators with higher resonance frequency, Q factor, and impedance, either off-chip [36] or on-chip [14], would result in larger dispersive shifts and hence improved signal-to-noise ratios.

The data that support the findings of this study are available from the corresponding author upon reasonable request.

ACKNOWLEDGMENTS

The work is supported by the European Union's Horizon 2020 research and innovation program under Grant Agreement No. 688539 (MOS-QUITO), by the European Research Council (ERC) Projects No. 759388 (LONGSPIN) and No. 810504 (QuCube), and by the French National Research Agency (ANR) projects MAQSi and CMOSQSPIN. S.Z. acknowledges support from an Early Postdoc.Mobility fellowship (P2BSP2_184387) from the Swiss National Science Foundation.

R.E. and S.Z. performed the experiments with help from R.M.; R.E., S.Z., R.M., and S.D.F. designed the experiment; L.H., B.B., and M.V. fabricated the sample; R.E. and S.Z. analyzed the results with input from V.M., J.L., A.A., Y.M.N., X.J., M.U., T.M., R.M., and S.D.F.; V.M. and J.L. established the theoretical analysis and simulations under the supervision of Y.M.N.; R.E., S.Z., V.M., R.M., and S.D.F. wrote the manuscript; M.S., X.J., M.V., and S.D.F. initiated the project.

APPENDIX A: THEORY

In this appendix we give the details of the theoretical analysis. In Sec. A1 we lay down the Hamiltonian of the double quantum dot. Then, in Sec. A2, we reduce this Hamiltonian to an effective two-level model that describes the driven dynamics of any pair of (M, N) and $(M + 1, N - 1)$ charge states. In Sec. A3, we introduce a model for the environment and compute the relaxation and dephasing rates that enter the master equations of Sec. A4. Then in Sec. A5 we compute the linear response function and the phase shift of the resonant circuit. In Sec. A6 we extend this description to the multilevel Hamiltonian of Sec. A1 at arbitrary magnetic field, and finally we include the resonant multiphoton processes in Sec. A7

1. Model of the driven double quantum dot

The double quantum dot system is resonantly driven by a fast electrical circuit with angular frequency ω_{exc} and probed by an LC circuit that is comparatively slow. The

dynamics of the double quantum dot is described by the Hamiltonian

$$\begin{aligned}
 H = & \hbar\omega_r \left(a^\dagger a + \frac{1}{2} \right) \\
 & + \sum_{i=1,2} \left[\hbar g_{ci} n_i (a + a^\dagger) + \varepsilon_i(t) n_i + \frac{U_i}{2} n_i (n_i - 1) \right] \\
 & + U_m n_1 n_2 - \sum_{\langle ij \rangle \sigma \sigma'} t_{i\sigma j \sigma'} c_{i\sigma}^\dagger c_{j \sigma'} \\
 & + \sum_{i=1,2} \frac{\mu_B}{2} (g_i \mathbf{B}_i) \cdot \boldsymbol{\sigma}_i + H_\kappa + H_\Gamma, \tag{A1}
 \end{aligned}$$

where a is the microwave photon operator, $c_{i\sigma}$ is the fermion operator for dot i and effective spin projection σ , $n_i = n_{i\downarrow} + n_{i\uparrow}$ is the occupation number of dot i , and $\boldsymbol{\sigma}_i$ is the vector whose components are the operators $\sum_{\sigma \sigma'} c_{i\sigma}^\dagger \sigma_{\alpha \sigma \sigma'} c_{i\sigma'}$, with σ_α ($\alpha = x, y$, and z) the Pauli matrices. The parameters of the model are

(a) the time-dependent energy potential on dot i , $\varepsilon_i(t) = e\alpha_{i1} V_{G1} + e\alpha_{i2} [V_{G2} + V_{\text{exc}}(t)]$ with V_{G1} , V_{G2} , and $V_{\text{exc}}(t) = V_{\text{exc}} \cos(\omega_{\text{exc}} t)$ the static and time-dependent voltages applied to gates 1 and 2, where $\alpha_{ij} > 0$ is the lever arm parameter between gate j and dot i , and $e > 0$ is the elementary charge;

(b) the spin-dependent charge tunneling matrix elements $t_{i\sigma j \sigma'}$ between the dots;

(c) the g tensor g_i and the magnetic field \mathbf{B}_i on dot i (μ_B being the Bohr magneton);

(d) the intradot Coulomb energies U_i and the interdot Coulomb energy U_m ;

(e) the natural frequency of the probe LC circuit $\omega_r = 1/\sqrt{L_r C_r}$, and the parameter of coupling between the dot charge and the quantum of the resonant circuit $\hbar g_{ci} = e V_{\text{rms}} \alpha_{i1}$, with $V_{\text{rms}} = \sqrt{\hbar \omega_r / (2C_r)}$ the zero-point voltage of the LC circuit [12].

The Hamiltonians H_κ and H_Γ describe the interaction of the environment with the LC circuit and double quantum dot, respectively.

2. Two-state model

Let us first analyze a two-state model that describes the dynamics of the double quantum dot in the vicinity of a single avoided crossing due to tunneling of a charge. We generalize to the multilevel double quantum dot in Sec. A6. Tunneling couples states with dot occupations (M, N) and $(M + 1, N - 1)$ that are detuned by the electrostatic energy $\varepsilon = \varepsilon_0 + (\alpha_{21} - \alpha_{11})eV_{G1} + (\alpha_{22} - \alpha_{12})eV_{G2} \equiv \varepsilon_0 - \alpha_1 eV_{G1} + \alpha_2 eV_{G2}$, where ε_0 is voltage independent (the detuning at zero gate voltages). Under driving, the time-dependent component of this detuning

is $A_{\text{exc}} \cos(\omega_{\text{exc}}t)$, with $A_{\text{exc}} = (\alpha_{22} - \alpha_{12})eV_{\text{exc}}$. Thus, the two-state Hamiltonian reads

$$H = -\frac{\varepsilon}{2}\sigma_z - \frac{\Delta}{2}\sigma_x - \frac{A_{\text{exc}}}{2}\cos(\omega_{\text{exc}}t)\sigma_z + \hbar\omega_r\left(a^\dagger a + \frac{1}{2}\right) + \hbar g_c \sigma_z (a + a^\dagger) + H_\kappa + H_\Gamma. \quad (\text{A2})$$

Here we use the Pauli matrix representation in the space of the charge configurations so that $\sigma_z \equiv n_1 - n_2$, σ_x describes tunneling (which opens an energy gap Δ), and the coupling parameter between the DQD charge and the microwave photon is

$$\hbar g_c = \frac{1}{2}(\alpha_{11} - \alpha_{21})eV_{\text{rms}} \equiv \frac{1}{2}\alpha_1 eV_{\text{rms}}. \quad (\text{A3})$$

The Hamiltonian (A2) is formally equivalent to the theory of Ref. [37]. Our aim is to adapt the model to the dispersive readout in our specific regime (Sec. A5) and to apply it to the spectroscopy of the multilevel system (Sec. A6). In the rotating frame of the driven system, Eq. (A2) can be transformed [37] to

$$\tilde{H} = \frac{\hbar\omega_R}{2}\sigma_z + \hbar\omega_r\left(a^\dagger a + \frac{1}{2}\right) + \hbar\tilde{\chi}\sigma_z\left(a^\dagger a + \frac{1}{2}\right) + \hbar\tilde{g}(\sigma_+ a + \sigma_- a^\dagger) + H_\kappa + \tilde{H}_\Gamma. \quad (\text{A4})$$

Here the effective coupling parameter reads

$$\tilde{g} = -g_c \cos\theta \frac{\omega_{R0}}{\omega_R}, \quad (\text{A5})$$

and the off-resonance frequency shift is

$$\tilde{\chi} = -\frac{2\hbar g_c^2 \sin^2\theta}{E} \frac{\delta\omega}{\omega_R}, \quad \hbar\omega_r \ll E. \quad (\text{A6})$$

The above equations feature the mixing factors $\cos\theta = \varepsilon/E$ and $\sin\theta = \Delta/E$, where $E = \sqrt{\varepsilon^2 + \Delta^2}$ is the energy spacing between the levels near the avoided crossing.

Furthermore, $\omega_R = \sqrt{\delta\omega^2 + \omega_{R0}^2}$ is the full Rabi angular frequency, with $\delta\omega = \omega_{\text{exc}} - E/\hbar$, $\omega_{R0} = A_{\text{exc}} \sin\theta/(2\hbar)$, and \tilde{H}_Γ describes the interaction of the system with the environment in the rotating frame. In our regime of parameters the interaction between the resonantly driven system and the probe circuit is well given by the rotating wave approximation (which is formally justified when $\omega_R - \omega_r \ll \omega_R + \omega_r$ [38,39]). We point out, though, that the off-resonance shift $\tilde{\chi}$ is taken in the adiabatic limit, which requires going beyond the rotating wave approximation [31,37–39].

3. Coupling to the environment

As a model of dissipation we consider the coupling between the active charge in the double quantum dot and bosonic modes that can be phonons or other modes of the environment with regular noise spectra that couple to the charge. In the charge basis the coupling between the system and its environment is described by the Hamiltonian

$$H_\Gamma = \sum_\alpha \hbar\omega_\alpha b_\alpha^\dagger b_\alpha + A\sigma_z \quad (\text{A7})$$

with $A = \sum_\alpha \lambda_\alpha (b_\alpha + b_\alpha^\dagger)$ and α being the index of the mode of the environment. Then the standard free evolution relaxation (Γ_\downarrow , Γ_\uparrow) and pure dephasing (Γ_φ) rates are

$$\Gamma_\downarrow = \frac{\sin^2\theta}{\hbar^2} S_{AA}\left(\frac{E}{\hbar}\right), \quad (\text{A8a})$$

$$\Gamma_\uparrow = \frac{\sin^2\theta}{\hbar^2} S_{AA}\left(-\frac{E}{\hbar}\right), \quad (\text{A8b})$$

$$\Gamma_\varphi = \frac{2\cos^2\theta}{\hbar^2} S_{AA}(0), \quad (\text{A8c})$$

with $S_{AA}(\omega)$ the noise correlation function [40].

4. Master equations

We describe the dynamics of the probed system semi-classically with Bloch master equations. In the same dressed basis set as Eq. (A4),

$$\langle \dot{\sigma}_- \rangle = -i\omega_R \langle \sigma_- \rangle - 2i\tilde{\chi} \langle \sigma_- (a^\dagger a + 1/2) \rangle + i\tilde{g} \langle \sigma_z a \rangle - \tilde{\Gamma}_2 \langle \sigma_- \rangle, \quad (\text{A9a})$$

$$\langle \dot{\sigma}_z \rangle = -2i\tilde{g} (\langle a\sigma_+ \rangle - \langle a^\dagger\sigma_- \rangle) - \tilde{\Gamma}_1 \langle \sigma_z \rangle + \tilde{\Gamma}_\uparrow - \tilde{\Gamma}_\downarrow. \quad (\text{A9b})$$

Here $\tilde{\Gamma}_2 = \tilde{\Gamma}_1/2 + \tilde{\Gamma}_\varphi$ is the total decoherence rate of the driven two-level system that includes the relaxation rate $\tilde{\Gamma}_1 = \tilde{\Gamma}_\downarrow + \tilde{\Gamma}_\uparrow$ and the pure dephasing rate $\tilde{\Gamma}_\varphi$. These rates differ from those for free evolution [Eq. (A8)] and are found [41,42] to be

$$\tilde{\Gamma}_{\downarrow/\uparrow} = \frac{(1 \mp \cos\eta)^2}{4} \Gamma_\downarrow + \frac{(1 \pm \cos\eta)^2}{4} \Gamma_\uparrow + \frac{1}{2} \sin^2\eta \Gamma_\nu, \quad (\text{A10a})$$

$$\tilde{\Gamma}_2 = \frac{3 - \cos^2\eta}{4} \Gamma_1 + \cos^2\eta \Gamma_\varphi + \frac{1}{2} \sin^2\eta \Gamma_\nu, \quad (\text{A10b})$$

where $\cos\eta = \delta\omega/\omega_R$ and $\sin\eta = \omega_{R0}/\omega_R$, $\Gamma_1 = \Gamma_\downarrow + \Gamma_\uparrow$ is the energy relaxation rate, and Γ_ν is proportional to the spectral function of the noise at the Rabi frequency

[41]. Within the environment model taken here, the rate Γ_v evaluates to

$$\Gamma_v = \frac{2 \cos^2 \theta}{\hbar^2} S_{AA}(\omega_R). \quad (\text{A11})$$

As derived in Refs. [41,42], these expressions for the rates assume that the environment temperature T is not too small (namely, $k_B T > \hbar\omega_R$).

In fact, the photon-number-dependent term in Eq. (A9a) is negligible in the linear regime and is already included in Eq. (A4) as an oscillator shift. Moreover, for a relatively weak coupling g_c , the first term on the right-hand side of Eq. (A9b) can be neglected and the slow probe resonator does not significantly change the average population of the states. We note that $D = -\langle\sigma_z\rangle = \tilde{P}_- - \tilde{P}_+$, the difference between the stationary occupation probabilities of the dressed ground and excited states, which becomes

$$D = \frac{\tilde{\Gamma}_\downarrow - \tilde{\Gamma}_\uparrow}{\tilde{\Gamma}_1}, \quad 4g_c^2 n_{\text{ph}} \ll \tilde{\Gamma}_1 \tilde{\Gamma}_2, \quad (\text{A12})$$

where n_{ph} is the average number of photons in the LC circuit. In this regime, with the relaxation rates defined above, we find that

$$D = \frac{-\cos \eta (\Gamma_\downarrow - \Gamma_\uparrow)}{(1 + \cos^2 \eta) \Gamma_1 / 2 + \sin^2 \eta \Gamma_v}. \quad (\text{A13})$$

This manifests population inversion in the dressed basis set for $\cos \eta > 0$ ($\delta\omega > 0$) [37].

5. Circuit phase response

We use input-output theory [32,39,40,43] to calculate the phase shift of the signal due to its interaction with the DQD. In the input-output approach the dynamics of the circuit mode is given by the quantum Langevin equation [43]. With Hamiltonian (A4), in the rotating frame of the incoming microwave photon of angular frequency ω_p (which is close to the natural angular frequency of the resonant circuit ω_r), the equation reads

$$\dot{a} = -i(\omega_r - \omega_p)a - i\tilde{\chi}\sigma_z a - i\tilde{g}\sigma_- - \frac{\kappa}{2}a - \sqrt{\kappa}b_{\text{in}}, \quad (\text{A14})$$

where κ is the escape rate of the photons and b_{in} is the incoming microwave photon field.

By solving Eq. (A9a) at frequency ω_p together with Eq. (A13), and using the input-output relations, we obtain the coefficient of reflection between the incoming and the

outgoing microwave signals,

$$r(\omega_p) = 1 + \frac{i\kappa}{\omega_r - \omega_p - i\kappa/2 + \chi(\omega_p)}, \quad (\text{A15})$$

where $\chi(\omega_p)$ is the charge response function at second order in the oscillator-DQD coupling:

$$\chi(\omega_p) = -\left(\tilde{\chi} + \frac{\tilde{g}^2}{\omega_R - \omega_p - i\tilde{\Gamma}_2}\right)D. \quad (\text{A16})$$

The real part of Eq. (A16) yields the linear shift of the resonator frequency. When $\omega_p = \omega_r$ and at linear order in the response function, we get the phase shift $\delta\phi = 4 \text{Re} \chi(\omega_r)/\kappa = 4Q \text{Re} \chi(\omega_r)/\omega_r$, with $Q = \omega_r/\kappa$ the quality factor of the LC resonator.

6. Double quantum dot spectroscopy

The above model naturally generalizes to multilevel systems, and we apply it to the spectroscopy of the double quantum dot. We diagonalize the part of Hamiltonian (A1) that does not include the drive and we thus obtain the energy levels and the corresponding states of the double quantum dot exactly. To calculate the response of the multilevel system, we sum Eq. (A16) over all excited states. For that purpose, we cast the mixing angle $\theta \equiv \theta_{\gamma\epsilon}$ for excited state $|\epsilon\rangle$ as matrix elements of the charge operators:

$$\sin \theta_{\gamma\epsilon} = \langle\gamma|(n_1 - n_2)|\epsilon\rangle = 2\langle\gamma|n_1|\epsilon\rangle = -2\langle\gamma|n_2|\epsilon\rangle, \quad (\text{A17a})$$

$$\cos \theta_{\gamma\epsilon} = \langle\gamma|n_1|\gamma\rangle - \langle\epsilon|n_1|\epsilon\rangle = -\langle\gamma|n_2|\gamma\rangle + \langle\epsilon|n_2|\epsilon\rangle. \quad (\text{A17b})$$

7. Multiphoton processes

The above analysis generalizes to multiphoton resonant processes. For the n -photon transition between levels γ and ϵ , we substitute [44]

$$\delta\omega \rightarrow \delta\omega^{(n)} = n\omega_{\text{exc}} - (E_\epsilon - E_\gamma)/\hbar, \quad (\text{A18})$$

$$\omega_{R0} \rightarrow \omega_{R0}^{(n)} = n\omega_{\text{exc}} |\tan \theta_{\gamma\epsilon}| J_n \left(\frac{A_{\text{exc}} |\cos \theta_{\gamma\epsilon}|}{\hbar\omega_{\text{exc}}} \right), \quad (\text{A19})$$

$$\omega_R \rightarrow \omega_R^{(n)} = \sqrt{(\delta\omega^{(n)})^2 + (\omega_{R0}^{(n)})^2}, \quad (\text{A20})$$

we denote by E_ϵ the energy of the excited state $|\epsilon\rangle$ and by E_γ the energy of the ground state $|\gamma\rangle$, where J_n is the n th Bessel function of the first kind. For small arguments, it approximates as $J_n(z) \approx (z/2)^n/n!$ ($z \ll 1$).

The total response is obtained by summing over all resonant photon processes $n = 1, 2, \dots$. In Fig. 5 we show the calculated response up to $n = 2$.

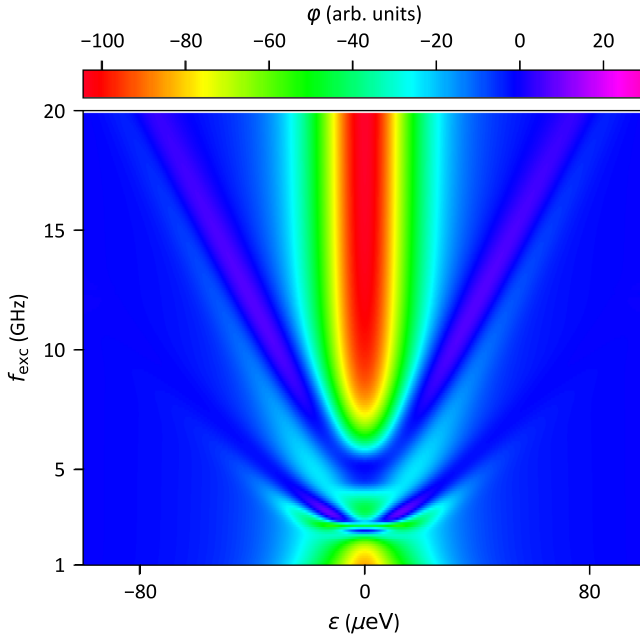


FIG. 5. Phase response of the driven double quantum dot as given by Eqs. (A15) and (A16) for the one- and two-photon processes at zero magnetic field. The parameters are $Q = 24$, $\hbar\omega_r = 2 \mu\text{eV}$, $\hbar g_c = 0.15 \mu\text{eV}$. The double quantum dot is modeled by the charge tunneling $t = 11.8 \mu\text{eV}$, tunneling with spin flip $t_{\text{SO}} = 8.3 \mu\text{eV}$, and g factors $g_1 = 4$, $g_2 = 1.91$. Detuning energy ε is counted from the point of charge degeneracy at zero magnetic field. The amplitude of the resonant drive is $A_{\text{exc}} = 15 \mu\text{eV}$. The phonon equilibrium temperature is significantly smaller than all energy separations between the levels, which corresponds to the limit $\Gamma_{\uparrow} \ll \Gamma_{\downarrow}$. With our environment model we set $S_{AA}(E_{\varepsilon} - E_{\gamma})/\hbar = S_{AA}(0)/\hbar = S_{AA}(\omega_R)/\hbar = 0.5 \mu\text{eV}$ for simplicity. To account for quasistatic noise due to the electrical environment, we furthermore convolute the computed signal with a Gaussian function of width $\sigma = 5 \mu\text{eV}$.

APPENDIX B: EXTRACTIONS

1. Tunnel coupling and spin-orbit interaction

In order to get a more precise and correct extraction of the tunnel coupling and the spin-orbit interaction, we need to take into account the impact of the charge noise fluctuations in our fitting model.

The transition frequency (f) of a charge qubit as a function of detuning (ε) is

$$f = \frac{\sqrt{\varepsilon^2 + \Delta^2}}{h}, \quad (\text{B1})$$

where h is the Planck constant and t is the tunnel coupling giving rise to an anticrossing gap Δ .

Low-frequency charge noise will lead to fluctuations of the qubit transition frequency. Assuming that the noise on the detuning axis is Gaussian, its probability density

function can be written as

$$\rho_{\varepsilon}(\varepsilon) = \frac{1}{\sigma_{\varepsilon}\sqrt{2\pi}} e^{-(1/2)(\varepsilon/\sigma_{\varepsilon})^2}, \quad (\text{B2})$$

where σ_{ε} is the standard deviation of the distribution of detuning noise. To transform the probability density function of the detuning noise into the probability density function for the transition frequency, we use the relation

$$\rho_y(y) = \rho_x[x(y)] \frac{dx(y)}{dy}, \quad (\text{B3})$$

where $\rho_y(y)$ is the probability density function of y and $y(x)$ is a function of x , whose probability density function is given by $\rho_x(x)$. Therefore, we find the following probability density function for the transition frequency:

$$\rho_f(f) = \begin{cases} 0, & f \leq \Delta/h, \\ \frac{2h^2f}{\sigma_{\varepsilon}\sqrt{2\pi}} \frac{e^{-(1/2)[(hf)^2 - \Delta^2]/\sigma_{\varepsilon}^2}}{\sqrt{(hf)^2 - \Delta^2}}, & f > \Delta/h. \end{cases} \quad (\text{B4})$$

The factor of 2 in $\rho_f(f)$ comes from the fact that there are two solutions to Eq. (B1) for $\varepsilon(f)$.

The linewidth of the qubit transition is given by the lifetime of the excited state (assuming that the ground state cannot decay and has infinite lifetime). From the Heisenberg uncertainty principle, we know that $\Delta E \Delta t \geq \hbar$ [45]. This directly translates into a spectral width $\Delta f = 1/(2\pi T_1)$, where T_1 is the lifetime of the excited state. Then, the full linewidth is described by a Lorentzian centered around frequency f_0 :

$$\mathcal{L}(f) = A \frac{(\Gamma/2)^2}{(f - f_0)^2 + (\Gamma/2)^2}. \quad (\text{B5})$$

Here A is the amplitude of the spectral ray at $f = f_0$ and $\Gamma = 1/T_1$ is the full width at half maximum and the lifetime of the excited state.

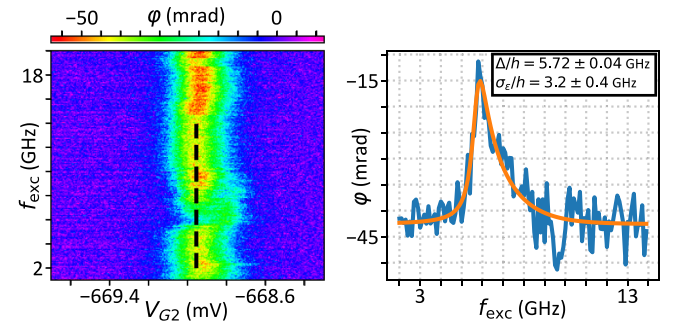


FIG. 6. Tunnel coupling extraction for ICT 2. Phase response of the LC resonator as a function of V_{G2} and f_{exc} is shown on the left, and a line cut (black dashed line) is shown on the right. The line cut is fitted with Eq. (B6) to extract the framed parameters.

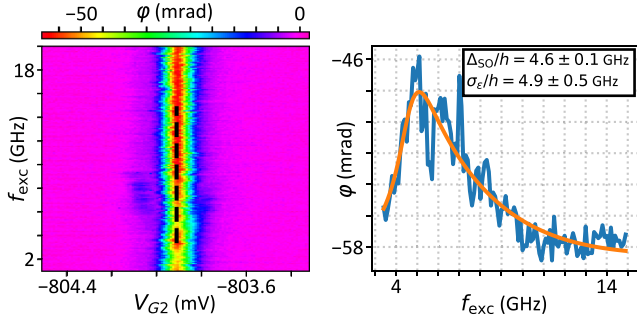


FIG. 7. Spin-orbit interaction extraction for ICT 1. Phase response of the LC resonator as a function of V_{G2} and f_{exc} is shown on the left, and a line cut (black dashed line) is shown on the right. The line cut is fitted with Eq. (B6) to extract the framed parameters.

The final lineshape of the phase response as a function of drive frequency at an anticrossing is given by the convolution of the intrinsic lineshape of the qubit (Lorentzian characterized by T_1) and the probability density function of the transition frequencies [21]:

$$\varphi(f) = \int_{-\infty}^{+\infty} \mathcal{L}(v) \rho_f(f - v) dv + \varphi_0 \quad (\text{B6})$$

with φ_0 a phase offset.

We compute Eq. (B6) numerically and pass it as the fitting model in order to extract the tunnel coupling at the anticrossing.

The fittings that allowed the extraction of Δ (in the case of ICT 2) and Δ_{SO} (in the case of ICT 1) are presented in Figs. 6 and 7, respectively. The dashed line cuts along the anticrossing detuning are taken from spectroscopy maps measured at the lowest constant room-temperature power.

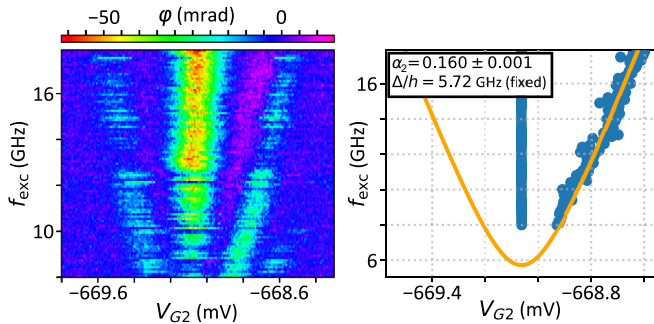


FIG. 8. Alpha factor extraction for ICT 2. Phase response of the LC resonator as a function of V_{G2} and f_{exc} (with power calibration) is shown on the left. The scatter plot on the right retraces the positions of the central line as well as the right dip-peak structure from the left graph. The orange curve is a fit using Eq. (B7) that yields the framed results.

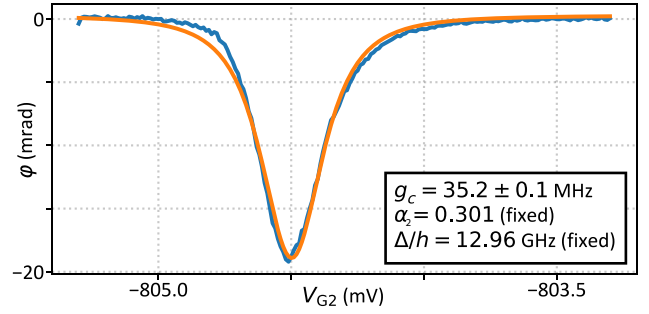


FIG. 9. Charge photon coupling extraction for ICT 1. The experimental data (blue) are fitted (orange) with Eqs. (1) and (2) to extract the relevant parameters.

2. Alpha factor

By following the center of the dip-peak structure of the wings, we get the energy gap value between the ground state and the excited state for each detuning value.

Figure 8 illustrates the extraction of the α factor. Starting from the calibrated spectroscopy map at zero magnetic field, we mark both the position of the central dip and the center of the wing dip-peak structure. We align afterwards the positions corresponding to zero detuning around their mean value V_0 . We can then fit alpha to the obtained wing positions with

$$hf_{\text{exc}} = \sqrt{\alpha_2^2 (V_{G2} - V_0)^2 + \Delta^2}, \quad (\text{B7})$$

where Δ is the anticrossing gap extracted as in Sec. B 1 and input in the model as a fixed parameter.

3. Charge photon coupling

The charge photon coupling is extracted using Eqs. (1) and (2) as a model. Each experimental dip in Figs. 9 and 10 is a 40 time average of the same measurement at zero magnetic field with no spectroscopy drive. We then fit these data while introducing the already extracted entities (α , t , Q , ...) as fixed parameters.

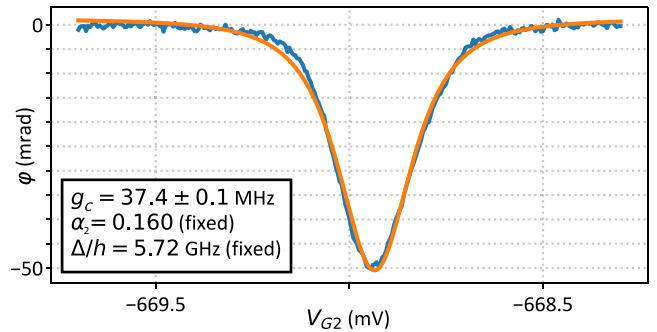


FIG. 10. Charge photon coupling extraction for ICT 2. The experimental data (blue) are fitted (orange) with Eqs. (1) and (2) to extract the relevant parameters.

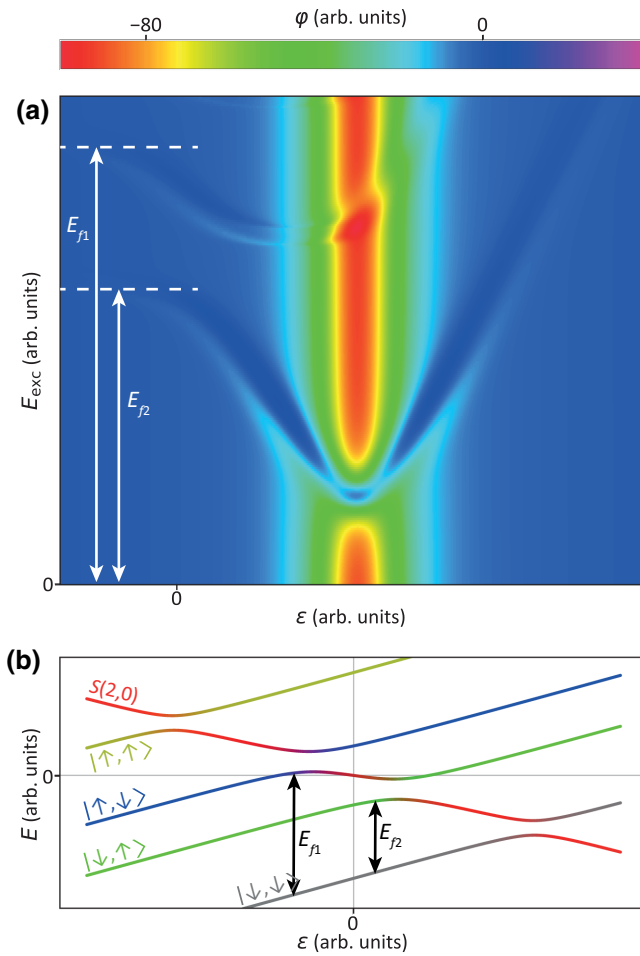


FIG. 11. The g -factor extraction. Simulated response of the driven DQD system at finite magnetic field in the case of an even charge parity (top panel) and the corresponding schematic of the energy diagram (bottom panel) highlighting the transition energies E_{f1} and E_{f2} necessary for g -factor extraction.

The decoherence rate Γ is neglected here since we assume that it is small compared to the tunneling.

4. g factors

Because of the g -factor difference between the two quantum dots, the Zeeman splitting induced by the applied magnetic field is not the same for both spins.

The energies E_{f1} and E_{f2} illustrated in Fig. 11 represent the energies necessary to respectively flip the spin of QD 1 and the spin of QD 2. These energies give access to the g factors knowing the applied magnetic field B since

$$E_{f1} = g_1 \mu_B B, \quad (\text{B8})$$

$$E_{f2} = g_2 \mu_B B, \quad (\text{B9})$$

where E_{f1} and E_{f2} are marked on a theoretical spectroscopy map in the top panel of Fig. 11.

- [1] D. Loss and D. P. DiVincenzo, Quantum computation with quantum dots, *Phys. Rev. A* **57**, 120 (1998).
- [2] J. Yoneda, K. Takeda, T. Otsuka, T. Nakajima, M. R. Delbecq, G. Allison, T. Honda, T. Kodera, S. Oda, Y. Hoshi, N. Usami, K. M. Itoh, and S. Tarucha, A quantum-dot spin qubit with coherence limited by charge noise and fidelity higher than 99.9%, *Nat. Nanotechnol.* **13**, 102 (2018).
- [3] M. Veldhorst, J. C. C. Hwang, C. H. Yang, A. W. Leenstra, B. de Ronde, J. P. Dehollain, J. T. Muhonen, F. E. Hudson, K. M. Itoh, A. Morello, and A. S. Dzurak, An addressable quantum dot qubit with fault-tolerant control-fidelity, *Nat. Nanotechnol.* **9**, 981 (2014).
- [4] M. Veldhorst, C. H. Yang, J. C. C. Hwang, W. Huang, J. P. Dehollain, J. T. Muhonen, S. Simmons, A. Laucht, F. E. Hudson, K. M. Itoh, A. Morello, and A. S. Dzurak, A two-qubit logic gate in silicon, *Nature* **526**, 410 (2015).
- [5] E. Kawakami, P. Scarlino, D. R. Ward, F. R. Braakman, D. E. Savage, M. G. Lagally, M. Friesen, S. N. Coppersmith, M. A. Eriksson, and L. M. K. Vandersypen, Electrical control of a long-lived spin qubit in a Si/SiGe quantum dot, *Nat. Nanotechnol.* **9**, 666 (2014).
- [6] R. Maurand, X. Jehl, D. Kotekar-Patil, A. Corna, H. Bohuslavskiy, R. Laviéville, L. Hutin, S. Barraud, M. Vinet, M. Sanquer, and S. De Franceschi, A CMOS silicon spin qubit, *Nat. Commun.* **7**, 13575 (2016).
- [7] H. Watzinger, J. Kukučka, L. Vukušić, F. Gao, T. Wang, F. Schäffler, J.-J. Zhang, and G. Katsaros, A germanium hole spin qubit, *Nat. Commun.* **9**, 3902 (2018).
- [8] N. W. Hendrickx, W. I. L. Lawrie, L. Petit, A. Sammak, G. Scappucci, and M. Veldhorst, A single-hole spin qubit, *Nat. Commun.* **11**, 3478 (2020).
- [9] N. W. Hendrickx, D. P. Franke, A. Sammak, G. Scappucci, and M. Veldhorst, Fast two-qubit logic with holes in germanium, *Nature* **577**, 487 (2020).
- [10] P.-A. Mortemousque, E. Chanrion, B. Jadot, H. Flentje, A. Ludwig, A. D. Wieck, M. Urdampilleta, C. Bauerle, and T. Meunier, Coherent control of individual electron spins in a two dimensional array of quantum dots, arXiv:1808.06180 (2018).
- [11] N. W. Hendrickx, W. I. L. Lawrie, M. Russ, F. van Riggelen, S. L. de Snoo, R. N. Schouten, A. Sammak, G. Scappucci, and M. Veldhorst, A four-qubit germanium quantum processor, arXiv:2009.04268 (2020).
- [12] A. Cottet, C. Mora, and T. Kontos, Mesoscopic admittance of a double quantum dot, *Phys. Rev. B* **83**, 121311 (2011).
- [13] J. I. Colless, A. C. Mahoney, J. M. Hornibrook, A. C. Doherty, H. Lu, A. C. Gossard, and D. J. Reilly, Dispersive Readout of a Few-Electron Double Quantum Dot with Fast rf Gate Sensors, *Phys. Rev. Lett.* **110**, 046805 (2013).
- [14] G. Zheng, N. Samkharadze, M. L. Noordam, N. Kalhor, D. Brousse, A. Sammak, G. Scappucci, and L. M. K. Vandersypen, Rapid gate-based spin read-out in silicon using an on-chip resonator, *Nat. Nanotechnol.* **14**, 742 (2019).
- [15] M. F. Gonzalez-Zalba, S. Barraud, A. J. Ferguson, and A. C. Betz, Probing the limits of gate-based charge sensing, *Nat. Commun.* **6**, 6084 (2015).
- [16] I. Ahmed, J. A. Haigh, S. Schaal, S. Barraud, Y. Zhu, C.-m. Lee, M. Amado, J. W. A. Robinson, A. Rossi, J. J. L. Morton, and M. F. Gonzalez-Zalba, Radio-Frequency Capacitive Gate-Based Sensing, *Phys. Rev. Appl.* **10**, 014018 (2018).

- [17] A. Crippa, R. Ezzouch, A. Aprá, A. Amisse, R. Laviéville, L. Hutin, B. Bertrand, M. Vinet, M. Urdampilleta, T. Meunier, M. Sanquer, X. Jehl, R. Maurand, and S. De Franceschi, Gate-reflectometry dispersive readout and coherent control of a spin qubit in silicon, *Nat. Commun.* **10**, 2776 (2019).
- [18] P. Pakkiam, A. V. Timofeev, M. G. House, M. R. Hogg, T. Kobayashi, M. Koch, S. Rogge, and M. Y. Simmons, Single-Shot Single-Gate rf Spin Readout in Silicon, *Phys. Rev. X* **8**, 041032 (2018).
- [19] M. Urdampilleta, D. J. Niegemann, E. Chanrion, B. Jadot, C. Spence, P.-A. Mortemousque, C. Bäuerle, L. Hutin, B. Bertrand, S. Barraud, R. Maurand, M. Sanquer, X. Jehl, S. De Franceschi, M. Vinet, and T. Meunier, Gate-based high fidelity spin readout in a CMOS device, *Nat. Nanotechnol.* **14**, 737 (2019).
- [20] A. West, B. Hensen, A. Jouan, T. Tanttu, C.-H. Yang, A. Rossi, M. F. Gonzalez-Zalba, F. Hudson, A. Morello, D. J. Reilly, and A. S. Dzurak, Gate-based single-shot readout of spins in silicon, *Nat. Nanotechnol.* **14**, 437 (2019).
- [21] Z. V. Penfold-Fitch, F. Sfigakis, and M. R. Buitelaar, Microwave Spectroscopy of a Carbon Nanotube Charge Qubit, *Phys. Rev. Appl.* **7**, 054017 (2017).
- [22] K. D. Petersson, C. G. Smith, D. Anderson, P. Atkinson, G. A. C. Jones, and D. A. Ritchie, Charge and spin state readout of a double quantum dot coupled to a resonator, *Nano Lett.* **10**, 2789 (2010).
- [23] A. Crippa, R. Maurand, L. Bourdet, D. Kotekar-Patil, A. Amisse, X. Jehl, M. Sanquer, R. Laviéville, H. Bohuslavskiy, L. Hutin, S. Barraud, M. Vinet, Y.-M. Niquet, and S. De Franceschi, Electrical Spin Driving by g -Matrix Modulation in Spin-Orbit Qubits, *Phys. Rev. Lett.* **120**, 137702 (2018).
- [24] F. N. M. Froning, L. C. Camenzind, O. A. H. van der Molen, A. Li, E. P. A. M. Bakkers, D. M. Zumbühl, and F. R. Braakman, Ultrafast Hole Spin Qubit with Gate-Tunable Spin-Orbit Switch, arXiv:2006.11175 (2020).
- [25] W. I. L. Lawrie, N. W. Hendrickx, F. van Riggelen, M. Russ, L. Petit, A. Sammak, G. Scappucci, and M. Veldhorst, Spin relaxation benchmarks and individual qubit addressability for holes in quantum dots, *Nano Lett.* **20**, 7237 (2020).
- [26] B. Voisin, V.-H. Nguyen, J. Renard, X. Jehl, S. Barraud, F. Triozon, M. Vinet, I. Duchemin, Y.-m. Niquet, S. de Franceschi, and M. Sanquer, Few-electron edge-state quantum dots in a silicon nanowire field-effect transistor, *Nano Lett.* **14**, 2094 (2014).
- [27] See Supplemental Material at <http://link.aps.org/supplemental/10.1103/PhysRevApplied.16.034031> for a complete measurement setup description, resonator characterization, the stability diagrams around ICT 1, and microwave line calibration.
- [28] T. Duty, G. Johansson, K. Bladh, D. Gunnarsson, C. Wilson, and P. Delsing, Observation of Quantum Capacitance in the Cooper-Pair Transistor, *Phys. Rev. Lett.* **95**, 206807 (2005).
- [29] M. A. Sillanpää, T. Lehtinen, A. Paila, Y. Makhlin, L. Roschier, and P. J. Hakonen, Direct Observation of Josephson Capacitance, *Phys. Rev. Lett.* **95**, 206806 (2005).
- [30] R. Mizuta, R. M. Otxoa, A. C. Betz, and M. F. Gonzalez-Zalba, Quantum and tunneling capacitance in charge and spin qubits, *Phys. Rev. B* **95**, 045414 (2017).
- [31] S. Park, C. Metzger, L. Tosi, M. F. Goffman, C. Urbina, H. Pothier, and A. L. Yeyati, From Adiabatic to Dispersive Readout of Quantum Circuits, *Phys. Rev. Lett.* **125**, 077701 (2020).
- [32] M. D. Schroer, M. Jung, K. D. Petersson, and J. R. Petta, Radio Frequency Charge Parity Meter, *Phys. Rev. Lett.* **109**, 166804 (2012).
- [33] M. Urdampilleta, A. Chatterjee, C. C. Lo, T. Kobayashi, J. Mansir, S. Barraud, A. C. Betz, S. Rogge, M. F. Gonzalez-Zalba, and J. J. Morton, Charge Dynamics and Spin Blockade in a Hybrid Double Quantum Dot in Silicon, *Phys. Rev. X* **5**, 031024 (2015).
- [34] M. G. House, T. Kobayashi, B. Weber, S. J. Hile, T. F. Watson, J. van der Heijden, S. Rogge, and M. Y. Simmons, Radio frequency measurements of tunnel couplings and singlet-triplet spin states in Si:P quantum dots, *Nat. Commun.* **6**, 8848 (2015).
- [35] X. Mi, C. G. Péterfalvi, G. Burkard, and J. R. Petta, High-Resolution Valley Spectroscopy of Si Quantum Dots, *Phys. Rev. Lett.* **119**, 176803 (2017).
- [36] D. J. Ibberson, T. Lundberg, J. A. Haigh, L. Hutin, B. Bertrand, S. Barraud, C.-M. Lee, N. A. Stelmashenko, J. W. A. Robinson, M. Vinet, M. F. Gonzalez-Zalba, and L. A. Ibberson, Large dispersive interaction between a CMOS double quantum dot and microwave photons, arXiv:2004.00334 (2020).
- [37] J. Hauss, A. Fedorov, C. Hutter, A. Shnirman, and G. Schön, Single-Qubit Lasing and Cooling at the Rabi Frequency, *Phys. Rev. Lett.* **100**, 037003 (2008).
- [38] D. Zueco, G. M. Reuther, S. Kohler, and P. Hänggi, Qubit-oscillator dynamics in the dispersive regime: Analytical theory beyond the rotating-wave approximation, *Phys. Rev. A* **80**, 033846 (2009).
- [39] S. Kohler, Dispersive readout: Universal theory beyond the rotating-wave approximation, *Phys. Rev. A* **98**, 023849 (2018).
- [40] A. A. Clerk, M. H. Devoret, S. M. Girvin, F. Marquardt, and R. J. Schoelkopf, Introduction to quantum noise, measurement, and amplification, *Rev. Mod. Phys.* **82**, 1155 (2010).
- [41] G. Ithier, E. Collin, P. Joyez, P. J. Meeson, D. Vion, D. Esteve, F. Chiarello, A. Shnirman, Y. Makhlin, J. Schrieffer, and G. Schön, Decoherence in a superconducting quantum bit circuit, *Phys. Rev. B* **72**, 134519 (2005).
- [42] J. Hauss, A. Fedorov, S. André, V. Brosco, C. Hutter, R. Kothari, S. Yeshwanth, A. Shnirman, and G. Schön, Dissipation in circuit quantum electrodynamics: Lasing and cooling of a low-frequency oscillator, *New J. Phys.* **10**, 095018 (2008).
- [43] C. Gardiner and P. Zoller, *Quantum Noise: A Handbook of Markovian and Non-Markovian Quantum Stochastic Methods with Applications to Quantum Optics* (Springer, Berlin, 2004), 3rd ed.
- [44] K. Ono, G. Giavaras, T. Tanamoto, T. Ohguro, X. Hu, and F. Nori, Hole Spin Resonance and Spin-Orbit Coupling in a Silicon Metal-Oxide-Semiconductor Field-Effect Transistor, *Phys. Rev. Lett.* **119**, 156802 (2017).
- [45] W. Demtröder, *Experimentalphysik 3: Atome, Moleküle und Festkörper*, Springer-Lehrbuch (Springer, Berlin Heidelberg, 2016).